ADVANCED FUNCTIONAL MATERIALS
www.afm-journal.de

Effect of 1-Fluoro-2-iodobenzene Solvent Additive on the Crystallization of Donors and Acceptors, and Ultrafast Carrier Dynamics in Polymer Solar Cells

Zezhou Liang, Lihe Yan, Ning Wang, Jinhai Si, Shujuan Liu, Yufei Wang, Junfeng Tong, Jianfeng Li, Baofeng Zhao, Chao Gao, and Xun Hou*

Controlled sequential crystallization of donors and acceptors is a critical factor for achieving enhanced phase separation and efficient charge transfer performance in polymer solar cells (PSCs). In this study, a comprehensive investigation of a structurally simple solvent additive, 1-fluoro-2-iodobenzene (OFIB) is conducted, which efficiently controls the morphology of the active layer, resulting in fibrous assembly and significantly enhancing the power conversion efficiency from 16.34% to 18.38% based on the PM6:L8-BO system. Density functional theory, molecular dynamics simulations, and grazing incidence small- and wide-angle X-ray scattering techniques reveal that the addition of OFIB to the processed blend aligns the orientation of the acceptor molecules, thereby enhancing the overall π–π stacking in the active layer. OFIB establishes nearly equal-strength π–π interactions with the conjugated frameworks of both the donor and acceptor materials, benefiting from the multiple electron conjugation between its iodine atom and the conjugated framework in the active layer. Femtosecond-timescale photophysical studies demonstrate that the OFIB-optimized active layer shows reduced exciton losses at the donor–acceptor interface. This study offers a new perspective on the mechanism underlying the function of solvent additives and presents a comprehensive research methodology that will guide the development of next-generation non-fullerene acceptors for efficient PSCs.

1. Introduction

Polymer solar cells (PSCs) have produced shockwaves in the field of renewable energy technology owing to their lightweight,[1,2] low-cost fabrication,[3–5] and mechanical flexibility.[6] The rapid development of high-performance donor and acceptor materials,[7] additives,[8,9] and interfacial buffer layers,[10–12] along with efficient processing techniques such as the layer-by-layer solution processing method,[13,14] has improved the maximum achievable power conversion efficiencies (PCEs) of PSCs to over 19% in single-junction devices.[15–17] The separation of photogenerated excitons and extraction of carriers are highly dependent on the size of the molecular packing and microscale phase separation in the bulk heterojunction (BHJ).[18–26] The purity and crystallinity of the donor- and acceptor-rich domains substantially influence the nanostructure of the BHJ, and consequently, the device performance.[27–30] Although these morphological features could enable sufficient donor/acceptor interfaces for exciton dissociation, they also introduce overmixed donor/acceptor phases into the active layer, which could hamper charge transport and collection during PSC operation, resulting in undesired charge recombination and preventing a further increase in PSCs performance.[31–33] Morphology control strategies,[34] such as thermal and vapor annealing,[35–37] hot-substrate casting,[38] and additive modulation,[16,39–42] have proven to be effective and essential methods for achieving high PCEs. However,

Z. Liang, L. Yan, N. Wang, J. Si, X. Hou
Key Laboratory for Physical Electronics and Devices of the Ministry of Education and Shaanxi Key Lab of Photonic Technique for Information
School of Electronics Science and Engineering
Faculty of Electronic and Information Engineering
Xi'an Jiaotong University
Xi'an 710049, P. R. China
E-mail: liheyan@mail.xjtu.edu.cn

The ORCID identification number(s) for the author(s) of this article can be found under https://doi.org/10.1002/adfm.202310312

DOI: 10.1002/adfm.202310312

S. Liu, B. Zhao, C. Gao
Xi'an Key Laboratory of Liquid Crystal and Organic Photovoltaic Materials
State Key Laboratory of Fluorine and Nitrogen Chemicals
Xi'an Modern Chemistry Research Institute
Xi'an 710065, P. R. China

Y. Wang
College of New Materials and New Energies
Shenzhen Technology University
Shenzhen 518118, P. R. China

J. Tong, J. Li
School of Materials Science and Engineering
Gansu Provincial Engineering Research Center for Organic Semiconductor Materials and Application Technology
Lanzhou Jiaotong University
Lanzhou 730070, P. R. China

it is difficult to precisely control the temperature during device processing, which reduces the reproducibility and stability of the device. Solvent additive engineering shows great promise for precisely adjusting nanomorphologies.[17]

Previous studies have reported the use of halogenated solvent additives in solution processing owing to their strong dipole moments and high boiling points.[43–45] These properties enable interactions with both donor and acceptor materials, leveraging the delayed evaporation characteristics of high-boiling solvents to extend the crystallization time and regulate the morphology of the donor–acceptor blend.[46–51] Solvent additives with strong dipole moments and molecular asymmetry have demonstrated favorable effects on PSCs.[52] Hou et al. proposed that volatilizable solid additives can enhance the intermolecular π–π stacking of non-fullerene acceptors, facilitating charge transport properties in the active layers, and resulting in improved efficiencies and stability of PSCs.[51] In addition, many aromatic solid additives with asymmetrically halogen-substituted benzene rings have been reported one after another, such as 1,3-dibromo-5-chlorobenzene.[16,52–58] In our recent research, we investigated the impact of three isomeric molecular additives on device performance, and all three halogenated additives significantly enhanced device performance.[7] Interestingly, the additives molecule with a dipole moment of zero achieved the highest device efficiency, which suggesting that the electrostatic induction effect of dipole moments may not be the sole explanation for active layer regulation. Such additives containing highly electronegative atoms or groups typically feature benzene rings or conjugated structures. However, there have been limited analyses on the specific interaction mechanisms between additives and donor or acceptor materials as well as their impact on photophysical mechanisms, such as π–π interactions as well as other potential dispersion forces. Non-fullerene acceptors (NFAs), in contrast to polymer donors, comprise small molecules with short conjugate lengths. Consequently, charge transport among NFAs is primarily influenced by conjugation and aggregation.[59,60] The ternary strategy, which involves the addition of a third component, can induce molecular aggregation to control the phase separation size.[6] For instance, in the case of "alloying" of donors or acceptors, the introduction of a third component can lead to a tight molecular stacking with the π-backbone of the donor or acceptor.[61] Thus, if an additive can induce the self-assembly of NFAs to achieve ordered head-to-tail stacking, the π–π stacking of NFAs will experience considerable enhancement.[60] The discovery of an additive that considers both the high boiling point of liquid additives, extending the crystallization time, and the benefits of solid additives, promoting π–π stacking and enhancing stability, will substantially advance the performance of PSCs, bringing them closer to industrialization.

In this study, we introduce a novel small molecules 1-fluoro-2-iodobenzene (OFIB), as shown in **Figure 1a**. The OFIB molecule contains fluorine (F) and iodine (I) atoms at the ortho position on the benzene ring. The F atom has the highest electronegativity, which significantly affects the electrostatic potential and dipole moment of the molecular surface. As the 53rd element in the fifth period of the periodic table, the I atom has an electron arrangement outside the nucleus of [Kr] $5s^2$ $4d^{10}$ $5p^5$. The electrons in the outermost orbit of the I atom, known as 5p orbital electrons, may have a multi-electron conjugation or p–π conjugation effect, enhancing the interaction between the OFIB and the donor/acceptor materials. The OFIB was selected as the solvent additives (melting point = −41 °C and boiling point = 189 °C), to achieve a well-defined fibril structure in the high-performance system of PM6:L8-BO, resulting in notably enhanced device PCE of 18.38%. We combined density functional theory (DFT) simulations with experimental results to analyze the interactions between the OFIB, donor, and acceptor materials. Despite the strong electronegativity of the fluorine atoms in OFIB, the resulting strong dipole moment is not a key factor contributing to the regulatory effect of OFIB on the active layer of PSCs. We propose that the excellent π–π interactions between OFIB and the donor/acceptor materials allow OFIB to act as a crystallization nucleus during the solvent evaporation process in the active layer, thereby inducing crystallization. Additionally, it is crucial to note that OFIB has other two isomers: (ortho-fluoroiodobenzene), meta-fluoroiodobenzene (MFIB), and para-fluoroiodobenzene (PFIB), we also examined the impact of isomerism effects on device performance.

2. Results and Discussion

Figure 1a shows the chemical structures of PM6, L8-BO, and the solvent additive OFIB. We first investigated the optical properties of neat and blended films processed with an OFIB or its counterpart. As shown in Figure 1b,c, the absorption profiles of PM6 and L8-BO processed with OFIB were clearly changed compared to their counterparts, with both maximum absorption peaks redshifted. The donor and acceptor absorption peaks could also be observed in the blend film with and without OFIB (as given by Figure S1a, Supporting Information). To study the origin of absorption peak change after the addition of OFIB, temperature dependent absorption experiments of neat L8BO, PM6, and PM6:L8-BO+OFIB film were performed. As shown in Figure S1b–d (Supporting Information), both the maximum absorption peaks were red shifted and the acromial absorption peaks obviously changed with the temperature increased. When the temperature increased, the crystallinity was enhanced and the molecules were packed closer, inducing the enhancement of π–π stacking. The decreased electrons transition energy from π to π^* orbitals caused the red shift of the maximum peak. The acromial absorption peak was attributed as "aggregation peak," which was also sensitive to the temperature.[31] The absorption near 400 nm changed slightly with the temperature, and this absorption was related to the vibration of the molecular skeleton (as show in the insert of Figure S1c,d, Supporting Information).

As shown in Figure 1d,e, we calculated the adsorption energy of OFIB with PM6 and L8-BO using the DFT. The final region of weak interaction between OFIB and PM6/L8-BO was obtained through a full-space conformational search, with green regions representing the area of interaction. The adsorption energy of OFIB:PM6 and OFIB:L8-BO was 21.86 and 20.68 kcal mol^{-1}, respectively. OFIB exhibited comparable adsorption energies with both PM6 and L8-BO. This similarity was due to the fact that interaction between OFIB and the donor or acceptor was primarily mediated through π–π stacking, so the difference in adsorption energy was insignificant. Figure 1f shows the natural bond orbital overlap between OFIB and PM6, revealing that the 5p orbital of the I atom was conjugated with the benzene ring on the side

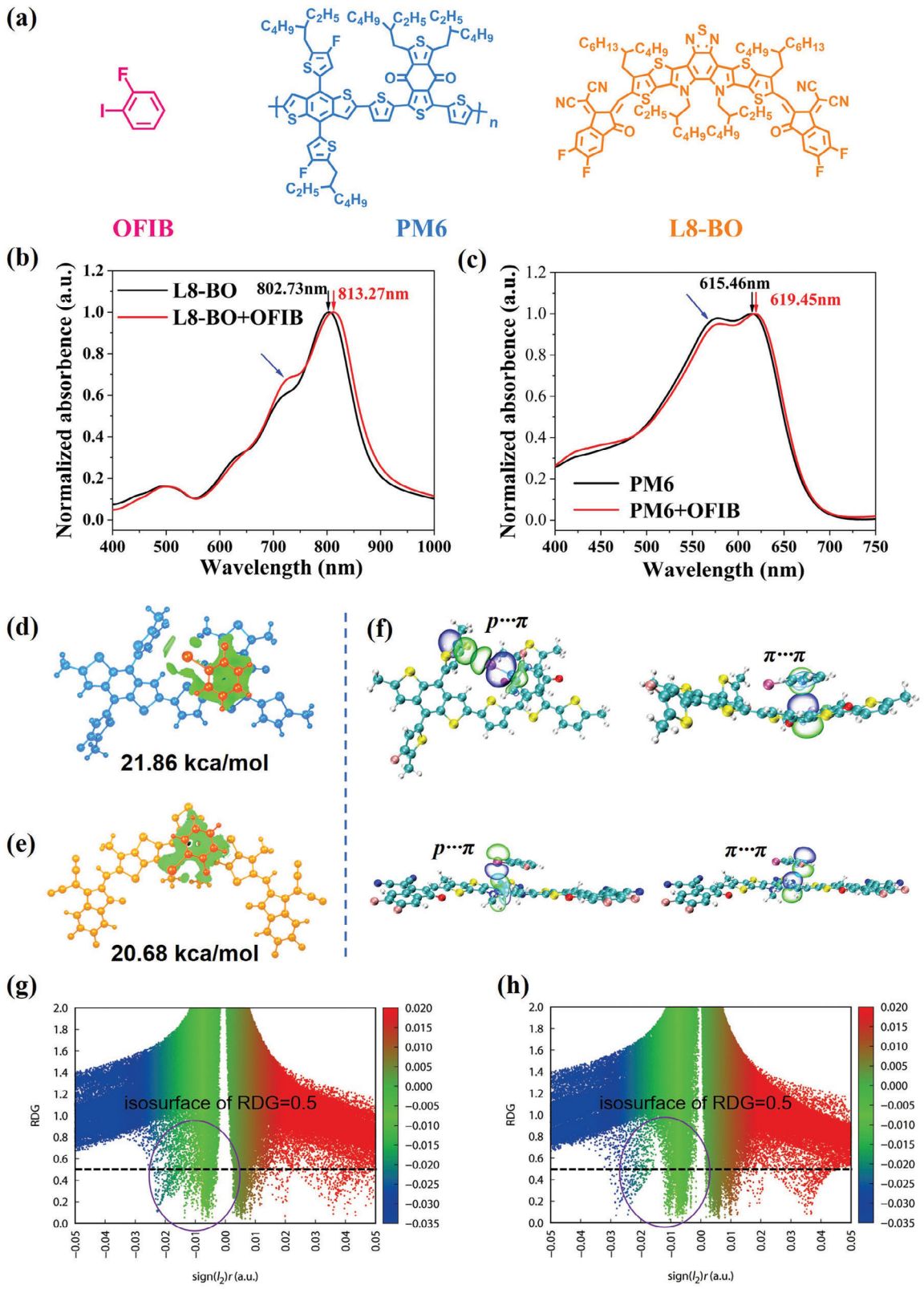

Figure 1. a) Molecular structures of the OFIB, PM6, and L8-BO; b,c) the UV spectrum of PM6 and L8-BO neat films processed with and without OFIB, respectively; d,e) the PM6 and L8-BO combined with the OFIB; f) the NBO analysis results; g,h) the sign$(\lambda_2)\rho$ and RDG functions for PM6+OFIB and L8-BO+OFIB dimer, respectively.

chain of BDT. OFIB and PM6 also exhibited π–π stacking effect. Similarly, OFIB:L8-BO demonstrated p–π conjugation and π–π stacking effect between each other. Furthermore, reduced density gradient (RDG) analysis was performed to qualitatively investigate the noncovalent interactions between OFIB and PM6/L8-BO. Figure 1g,h shows the RDG scatter plot, where the green and blue regions of the RDG analysis indicated the presence of marked non-covalent attractive interactions between the OFIB and PM6/L8-BO. RDG analysis in Figure 1g,h revealed distinct features within the range of x-axis −0.03 to −0.01. This suggested that the contribution of van der Waals forces between OFIB and PM6 was relatively higher than the weak van der Waals interaction between OFIB and L8-BO.[52] This also elucidated the slight elevation in the adsorption energy of OFIB with PM6. This characteristic of relatively balanced adsorption energies for the OFIB, along with both the donor and acceptor, could be exploited to control the phase separation size and molecular packing. As shown in Figure S2 (Supporting Information), according to the DFT calculation and the IGM analysis, both the MFIB and PFIB displayed the interaction styles between the additives molecular and the PM6/L8BO, which was similar to OFIB. The absorption energy of additives molecular between PM6 were: OFIB (21.86 kcal mol^{-1}) ≈ MFIB (21.89 kcal mol^{-1}) > PFIB (21.38 kcal mol^{-1}); and the absorption energy of additives molecular between L8-BO were: OFIB (20.68 kcal mol^{-1}) ≈ MFIB (18.93 kcal mol^{-1}) > PFIB (18.42 kcal mol^{-1}). The OFIB had the strongest weak interaction force between PM6 and L8-BO compared with MFIB and PFIB. This may be related to the dipole moment size of the additive molecules (Figure S3, Supporting Information), for OFIB, MFIB, and PFIB with the dipole moment of 2.296 (Debye), 1.488 (Debye), and 0.084 (Debye), respectively. This characteristic of relatively balanced adsorption energies for the OFIB, along with both the donor and acceptor, could be exploited to control the phase separation size and molecular packing.

The thermogravimetry analysis was employed here to examine the OFIB processed PM6:L8-BO blend, and a distinct 5% weight loss at about 66.5 °C and a low volatilized temperature of 100 °C were observed. It exhibits the OFIB could be easily removed by thermal or vacuum annealing (Figure S4, Supporting Information). Moreover, after the thermal annealing treatment, no signal of I 3d was observed in the X-ray photoelectron spectrometer spectra of the PM6:L8-BO films with the OFIB treatment, confirming the high volatility (Figure S5a,b, Supporting Information). The miscibility between PM6, L8-BO, and OFIB was investigated by calculating the surface free tension (γ) via measuring the contact angles based on water and diiodomethane drop-lets on the substrates, as displayed in Figure S6 and Table S1 (Supporting Information). PM6 demonstrated a lower γ value (27.04 mN m^{-1}) that L8-BO (37.53 mN m^{-1}) and OFIB (59.27 mN m^{-1}), respectively. The Flory–Huggins interaction parameter (χ) calculated from the surface energy (γ) is a critical parameter for measuring the miscibility between two materials, suggesting that a small χ value indicates that the two materials mix better, the calculated details are summarized in the Supporting Information. Additionally, the calculated χ for PM6:OFIB is 6.24 K, which was much higher than the values for the L8-BO:OFIB (2.47 K) and PM6:L8-BO (0.85 K) blends.

To validate this hypothesis, we used grazing-incidence wide-angle X-ray scattering (GIWAXS) measurements to examine the impact of OFIB on the molecular crystallinity and intermolecular interactions in the PM6 and L8-BO films, and the results are summarized in Table S2 (Supporting Information). **Figure 2**a,b shows the 2D GIWAXS scattering patterns and the corresponding out-of-plane (OOP) and in-plane (IP) line cuts of the neat films. The PM6 neat film exhibited clear (010) and (100) diffraction peaks in both the OOP and IP directions, suggesting a mixture of edge-on and face-on orientations. The (010) diffraction peak in the OOP direction was located at q_z = 1.667 Å^{-1} and corresponded to a π–π stacking distance of 3.768 Å. The crystal coherence lengths (CCLs) of the (010) diffraction peaks in the OOP direction for the neat PM6 films were estimated to be 20.204 Å. The corresponding data are presented in **Table 1**. After being processed with OFIB, the (010) diffraction peak of the PM6 films shifts to q_z = 1.683 Å^{-1}, corresponding to a π–π stacking distance of 3.732 Å, with CCLs of 23.149 Å. In addition, the intensities in the OOP direction are enhanced. Additionally, similar substantial crystallization changes were observed in films based on OFIB-processed L8-BO. Compared with the control L8-BO film, the (010) diffraction peak shifted from 1.706 to 1.752 Å^{-1} and corresponded to a smaller π–π stacking distance of 3.584 Å. This shift indicated closer molecular packing and stronger intermolecular π–π interactions. Additionally, the CCL of the OFIB-processed L8-BO films increased from 14.290 to 16.729 Å.

Y-series NAFs, consisting of banana-shaped molecules, extended their conjugation through end-group stacking, forming a zigzag polymer-like conjugated backbone. In the crystal lattice, these 1D channels were formed by the (110) lattice plane and extended along the cube-body diagonal. For the molecules in the blends, slight variations in the intermolecular distances and molecular conformations substantially affected the mobility of electrons and holes (Figure S7, Supporting Information).[62] The physical picture of charge transfer in organic semiconductors is often influenced by positional disorder and polarization effects, making it difficult to evaluate these contributions experimentally. This issue could be addressed by combining simplified models with quantum chemical calculations. According to the Marcus charge-transfer theory, the Marcus charge-hopping rate was expressed in formula (1):[62,63]

$$k = \frac{2\pi}{\hbar} J^2 \frac{1}{\sqrt{4\pi\lambda k_B T}} \exp\left(-\frac{\lambda}{4k_B T}\right) \quad (1)$$

where the λ represents the reorganization energy, J represents the transfer integral, and $\hbar$ reduces Planck's constant. The reorganization energy is the sum of internal reorganization energy λ_i and external reorganization energy λ_S. Furthermore, the λ_i accounts for the reorganization of the molecular geometry upon oxidation or reduction, the λ_S accounts for the polarization due to the environment of the molecule, the λ_S is much smaller than the λ_i usually. A large transfer integral and small reorganization energy produce a maximized hopping rate. λ_i is related to the intrinsic properties of molecules. Here, we calculated the charge transfer integral by estimating the direct interaction between the orbitals of the molecules involved in charge transfer ($\psi_{i,j} \equiv$ HOMOs or LUMOs) $\psi_i|H|\psi_j$, with this matrix element calculated in an orthogonal $\{\psi_i\}$ basis set.[62] As shown in Figure 2c–e, we calculated the electron and hole transfer integrals as a function of the scan distance for the L8-BO:L8-BO, PM6:PM6, and PM6:L8-BO

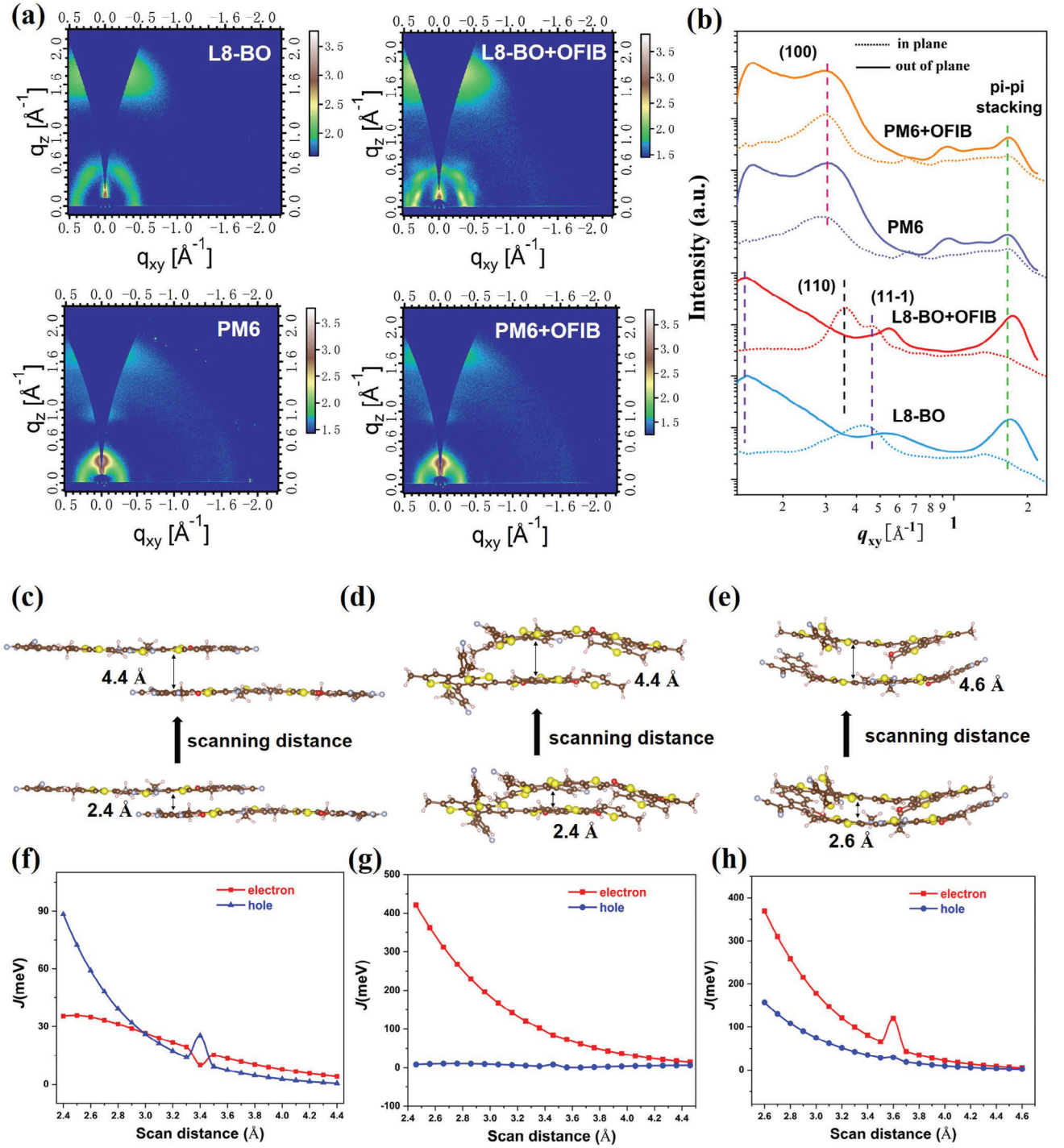

Figure 2. a) 2D Grazing incidence wide-angle X-ray scattering (GIWAXS) patterns and b) corresponding out-of-plane and in-plane line cuts of PM6 and L8-BO neat films processed with and without OFIB. The schematic diagram of calculation of charge transfer integral and the relationship of charge transfer integral between electron and hole: c,f) for L8-BO dimer, d,g) for PM6 dimer, and e,h) for PM6:L8-BO dimer, respectively.

dimers, respectively. The scan of the dimers was along the arrows in the picture show the direction, with step sizes of 0.1 Å, and Figure S8 (Supporting Information) exhibits the top view of the three dimers. The calculated results indicated that the transfer integral was highly sensitive to the molecular stacking distance, as shown in Figure 2f–h. When the distance between the two molecules moved to near the equilibrium position, the electronic wave function could become more sensitive, and sudden changes of the charge transfer integral at ≈3.4 Å were observed. Unlike the other two dimers, the hole transfer integral of the L8-BO:L8-BO

Table 1. Photovoltaic parameters of the as cast and 0.65% (Vol) OFIB processed PM6:L8-BO-based devices, and five devices were fabricated for each condition.

Active layer	Conditions	V_{OC} [V]	J_{SC} [mA cm^{-2}]	FF [%]	PCE [%]	PCE$_{max}$ [%]
PM6:L8-BO	w/a	0.92	24.76 ± 0.2	72.14 ± 0.5	16.15 ± 0.1	16.34
	0.65% OFIB	0.91	25.66 ± 0.2	79.15 ± 0.5	18.25 ± 0.1	18.38

dimer appeared to be more sensitive than the electron transfer integral at shorter distances. Both the PM6:PM6 and PM6:L8-BO dimers were more sensitive to electron transfer integration. The abrupt changes in the electron and hole charge transfer integrals were due to changes in the molecular orbital overlap with distance, as shown in Figure 2f,h. The larger spread of the hole transfer integral as a function of distance was explained by a larger positional disorder, which also reflected the larger width of the Gaussian density of states of the HOMO orbit for the Gaussian disorder model. Therefore, reducing the π–π stacking distance between molecules effectively improves the charge transfer between molecules and further promotes carrier transport.

Solar cell devices were fabricated using an indium tin oxide (ITO)/poly(3,4-ethylenedioxythiophene):poly(styrenesulfonate) (PEDOT:PSS)/PM6:L8-BO/PDINN/Ag structure. The current density–voltage (J–V) curves are shown in **Figure 3a**, and the detailed parameters are summarized in Table 1 and Figure S9 (Supporting Information). The control device using CF as the solvent without any additives achieved a maximum PCE of 16.34% with an open-circuit voltage (V_{OC}) of 0.92 V, a short-circuit current (J_{SC}) of 24.76 mA cm^{-2}, and a fill factor (FF) of 72.14%. The devices processed with 0.65% OFIB achieved a maximum PCE of 18.38% with a V_{OC} of 0.91 V, a J_{SC} of 25.66 mA cm^{-2}, and an FF of 79.15%. Compared with 0.50% and 0.65% OFIB-processed devices, the 1% OFIB-processed devices achieved a lower V_{OC} with a slightly changed J_{SC}. This may be attributed to excessive phase separation in the active layer due to an increased ratio of additives, accelerating charge transfer and recombination between the donor and acceptor, thereby causing changes in the V_{OC}. Further investigation was conducted in the subsequent section on molecular dynamics simulations. The devices processed with 0.50% PFIB achieved a maximum PCE of 17.22% with a V_{OC} of 0.86 V, a J_{SC} of 26.14 mA cm^{-2}, and an FF of 78.72% (Figure S10a, Supporting Information). And the devices processed with 0.65% MFIB achieved a maximum PCE of 14.91% with a V_{OC} of 0.87 V, a J_{SC} of 24.71 mA cm^{-2}, and an FF of 69.30% (Figure S10b, Supporting Information). Therefore, OFIB has better performance to optimize OSCs than MFIB and PFIB (Table S4, Supporting Information). The external quantum efficiency (EQE) spectra of the PM6:L8-BO-based devices are shown in Figure 3b, which exhibit a broad and strong photo response from 300–950 nm. The devices processed with OFIB exhibit a higher EQE response than the control devices in the 400–800 nm range, and the calculated integral current densities are 25.13 and 24.03 mA cm^{-2}, respectively, which agree well with the J–V measurements. The photocurrent density (J_{ph}) versus effective bias (V_{eff}) characteristics were measured to evaluate the exciton dissociation probability P(E,T) in the PSCs under short-circuit conditions. As shown in Figure 3c, P(E,T) can be determined by dividing the J_{ph} recorded under short-circuit conditions by the saturated photocurrent (J_{sat}) recorded with a high V_{eff}. For the control devices, J_{sat} is 26.19 mA cm^{-2} with P(E,T) of 94.53%, and for the OFIB processed devices, J_{sat} is 26.51 mA cm^{-2} with P(E,T) of 96.79%. The calculated maximum exciton generation rates G_{max} for the control and OFIB-processed devices were 1.36×10^{23} and 1.38×10^{23} m^{-3} s^{-1}, respectively. This indicates that the OFIB-processed devices are beneficial for obtaining higher photocurrents.

In this study, the optical transmission matrix method was employed to simulate exciton generation in the active layer, which could be influenced by additives.[64,65] We assumed that the active-layer film of the solar cell was a homogeneous dielectric film and that the interface was parallel and smooth. Light incident on the film was described as a plane wave. The photogenerated excitons dissociate at the interface and the range of exciton diffusion does not depend on the excitation energy. The complex refractive indices of the control and OFIB-processed films are shown in Figure S11 (Supporting Information). In addition, all excitons dissociate into charges. The simulated device structure consisted of ITO (180 nm)/PEDOT:PSS (30 nm)/active layer (120 nm)/PDINN (30 nm)/Al (100 nm). For a multilayered system, the energy distribution Q of each layer was explicitly a function of the wavelength λ and position x, which was calculated by the formula (2):[65]

$$Q(x,\lambda) = \frac{1}{2} c\varepsilon_0 \alpha n \left| E(x) \right|^2 \tag{2}$$

where c is the speed of light, ϵ_0 is the permittivity of free space, α is the absorption coefficient, n is the refractive index, and $E(x)$ is the optical electric field. Therefore, the calculated squared optical electric field strength $|E(x)|^2$ distribution within the solar cells can help investigate the reason for the enhancement of J_{SC}. Figure 3d shows the squared electric field intensity ($|E(x)|^2$) distribution relative to the position and absorption spectrum wavelength of the active layer. By comparing the normalized $|E(x)|^2$ for the control and OFIB-processed devices, we found that the electric field intensity increased at wavelengths of 450, 620, 720, and 810 nm after using the OFIB (Figure S7a,b, Supporting Information). The stronger $|E(x)|^2$ could be due to the OFIB-processed devices with stronger interference from the multilayers, which suggested uniform molecular packing. Figure 3e and Figure S7c,d (Supporting Information) show the simulated photogeneration rate distributions relative to their positions and the absorption spectrum wavelength of the active layer. The OFIB-processed blend exhibited a specifically wider wavelength response and a greater exciton production rate with position distribution. The maximum photogeneration rate of the control and OFIB-processed blend films were 1.32×10^{22} and 1.58×10^{22} s^{-1} cm^3, respectively, which suggested that the excitons were more abundant in the active layer using OFIB.

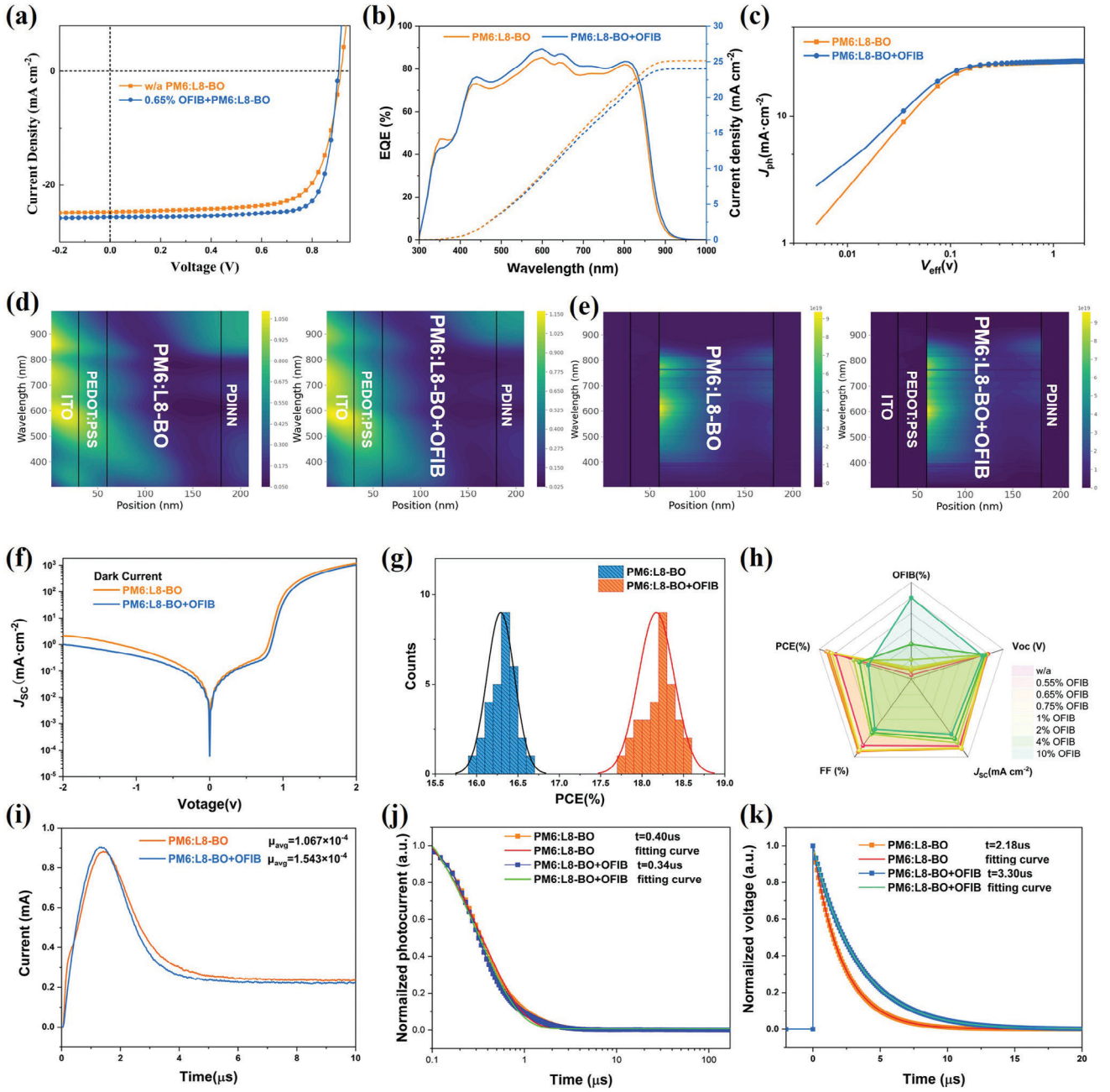

Figure 3. a) *J*–*V* curves of PM6: L8-BO-based devices; b) EQE spectra of devices; c) Photocurrent density (J_{ph}) versus effective voltage bias (V_{eff}) characteristics; d) Squared electric field intensity ($|E(x)|^2$) distribution at different wavelengths and position; e) Photogenerated excitons distribution at different wavelengths and position; f) The current density under the dark condition; g) The efficiency normal distribution diagram of the device; h) The spider diagram of photovoltaic parameters; i) Photo-CELIV curves of the solar cell devices used to calculate the carrier mobilities; and j,k) Normalized transient photocurrent and transient photovoltage traces of the optimal devices, respectively.

Figure 3f shows the dark *J*–*V* curves of the devices, revealing that the OFIB-processed devices exhibited substantially lower current densities at reverse biases than the control device. This result suggested larger rectification ratios and improved diode quality of the devices after the OFIB processing, which was expected to effectively suppress charge recombination. The hole and electron mobilities were calculated using the space-charge-limited current method (Figure S13, Supporting Information). The hole (μ_h) and electron (μ_e) mobility were increased from 7.22×10^{-4} and 5.70×10^{-5} to 1.10×10^{-3} and 7.67×10^{-4} $cm^2 V^{-1} s^{-1}$, respectively, both the hole and electron mobilities were increased. Furthermore, the charge recombination mechanism of the two devices was evaluated to investigate the relationship between light intensity (P_{light}) and J_{SC}, which follows a power–law equation of $J_{SC} \propto P_{light}^{\alpha}$. As shown in Figure S14 (Supporting Information), the control and OFIB-processed devices had

α values of the control and OFIB-processed devices were 0.928 and 0.963, respectively. Values closer to 1 indicated lower bimolecular recombination.[11,12] Figure 3g shows the statistics of solar cell devices, and significant differences could be seen from control and OFIB-processed devices. Device performance presented a normal distribution, and a PCE ≈18.3% of the optimized OFIB-processed device. Figure 3h shows the association of OSCs performance with the OFIB content, as well as the device parameters of PCE, V_{OC}, J_{CS}, and FF. We then conducted photon-induced charge-carrier extraction in linearly increasing voltage measurements to evaluate the device mobility. Based on the plots presented in Figure 3i, the device with OFIB processing exhibits a calculated mobility of 1.54×10^{-4} cm^2 V^{-1} s^{-1}, which slightly exceeded that of the control device (1.07×10^{-4} cm^2 V^{-1} s^{-1}). To investigate the charge-recombination behavior of the devices, measurements were conducted under open-circuit conditions. Figure 3j shows the results of transient photocurrent (TPC) measurements unveiling the lifetimes of the charge carriers. The TPC decay values of the control devices (0.40 µs) were slightly longer than that of the OFIB-processed device (0.34 µs). These results indicated a faster turn-off dynamic in OFIB-processed devices, implying a lower trap-state density. In addition, to study the charge-recombination behavior of the devices, transient photovoltage (TPV) measurements were conducted. The TPV decay values of the control and OFIB-processed devices are 2.18 and 3.30 µs, respectively (as shown in Figure 3k). These results indicated that the utilization of the OFIB aided in suppressing charge recombination, which was advantageous for enhancing the PCE. The recombination time of the photogenerated carriers was determined by fitting the transient photovoltage decay curves using a monoexponential decay function. Furthermore, the OFIB also showed a good universality in other Y-series NAFs systems, such as PM6:Y6 and PM6:BTP-eC9 (Figures S15 and S16, and Tables S5 and S6, Supporting Information) were optimized with OFIB exhibited PCE of 17.01% and 17.69%, respectively.

To understand the origin of the device performance enhancement by adding the OFIB, the microstructures of the blend films were further investigated. **Figure** 4a–d shows the atomic force microscopy (AFM) and transmission electron microscopy (TEM) results for the control and OFIB-processed blend films. After adding OFIB, the root mean square surface roughness of the blend films decreased from 1.24 to 1.06 nm, and a fibril network structure was observed in the OFIB-processed blend film. According to the previous reports, the fiber-like structures were mainly contributed by the donor phase.[66] The formation of the fibril network structure revealed the better phase-separation of the donor and acceptor in the blend film, which was beneficial to the exciton dissociation and charge transport in OSCs. In the early stage of film formation, the solvent evaporated gradually, and PM6 and L8BO crystallized separately under the induction of OFIB forming better phase separation. The OFIB acted as a nucleating agent to induce crystallization during the film crystallization process, thereby controlling the morphology of the film at a microscopic scale. The AFM was employed to further investigate the 0.5% PFIB and 0.65% MFIB processed PM6:L8-BO morphology, and the root mean square surface roughness were 2.32 and 3.93 nm, respectively, and no fibril network structure were observed (as shown in Figure S17, Supporting Information). Moreover, due to MFIB's significantly lower boiling point (77–78 °C) than OFIB (188–189 °C) and PFIB (182.8 °C), the fast evaporation during the film formation could lead to the shortest time frame for controlling the active layer's morphology. The poor morphology of MFIB processed PM6:L8-BO blend could cause the lower device performance. GIWAXS was used to investigate the crystallinity of the blended films. Based on the (010) diffraction peaks in the OOP direction and the (100) diffraction peaks in the IP direction, both the control and OFIB-processed films exhibited predominantly face-on orientations (Figure 4e–g). The OFIB-processed blend film exhibits a slightly enhanced (010) π–π stacking peak intensity in the OOP direction, along with a larger CCL of 17.98 Å, compared to the control blend film, which had a CCL of 16.94 Å (Table S7, Supporting Information). Additionally, the (010) π–π stacking peak of the OFIB-processed film experienced a slight shift from 1.688 to 1.709 Å in comparison to the control film, indicating enhanced π–π interactions in the OFIB-processed blend. The blend films, both control and OFIB-processed, exhibited lamellar stacking peaks at 0.302 Å^{-1} (20.733 Å) and 0.309 Å^{-1} (20.308 Å) in the IP direction, indicating that the effect of OFIB on lateral molecular backbone-to-backbone separation was minimal. In Figure 4h, we compared the CCL of the controlled and OFIB-processed blend in IP and OOP direction. The CCL of the OFIB-processed blend increased from 16.94 to 17.98 Å in IP direction, but decreased from 78.02 to 72.63 Å in OOP direction when compared to the control blend. The optimized blend morphology obtained through OFIB could make the carriers easier to be extracted by the electrode. Figure 4i–k shows the GISAXS intensity profiles. The scattering contributions from the pure phase size ($2R_g$) and the intermixing domain size (ξ) were fitted using the fractal-like network model and the Debye–Anderson–Brumberger model, respectively. The $2R_g$ values of the control and OFIB-processed blends were 9.3 and 11.1 nm, respectively (Table S8, Supporting Information). The increased ordering of the respective domains could be attributed to the introduction of additives during crystallization. Additionally, the ξ of the OFIB-processed blend (31.3 nm) was larger than that of the control blend (28.8 nm), which supported the improved FF and J_{SC}.

To gain further insight into the effect of OFIB on molecular packing, MD simulations were performed. The molecular packing of the control and OFIB-processed blend films was simulated, and snapshots are shown in **Figure** 5a–c. The center-of-mass radial distribution functions (RDFs) of the BDT core of PM6 relative to those of L8-BO are shown in Figure 5d. The first peak of $g(r)$ in PM6:L8-BO+OFIB blend indicated a significant increase in the probability or proportion of L8-BO distribution around BDT at ≈0.28 nm, compared with the first $g(r)$ in the PM6:L8-BO system which appearing at around 0.38 nm. This implied that in the OFIB-processed blend, the molecular orientation of L8-BO around BDT at 0.28 nm was likely to be more uniform, leading to a denser distribution between acceptor molecules, which might contribute to the enhancement of π–π stacking. Although the interaction between the donor and acceptor enhanced the coupling for electron transfer, it simultaneously resulted in unfavorable energetic states and recombination, especially when the BDT unit was in close proximity to the receptor. These factors contributed to the decrease in the V_{OC} and J_{SC} of the devices.[66,67] Consequently, the simulated results also accounted for the slight decrease in the device voltage. Figure 5e shows the center-of-mass RDFs of L8-BO:L8-BO for the two blended

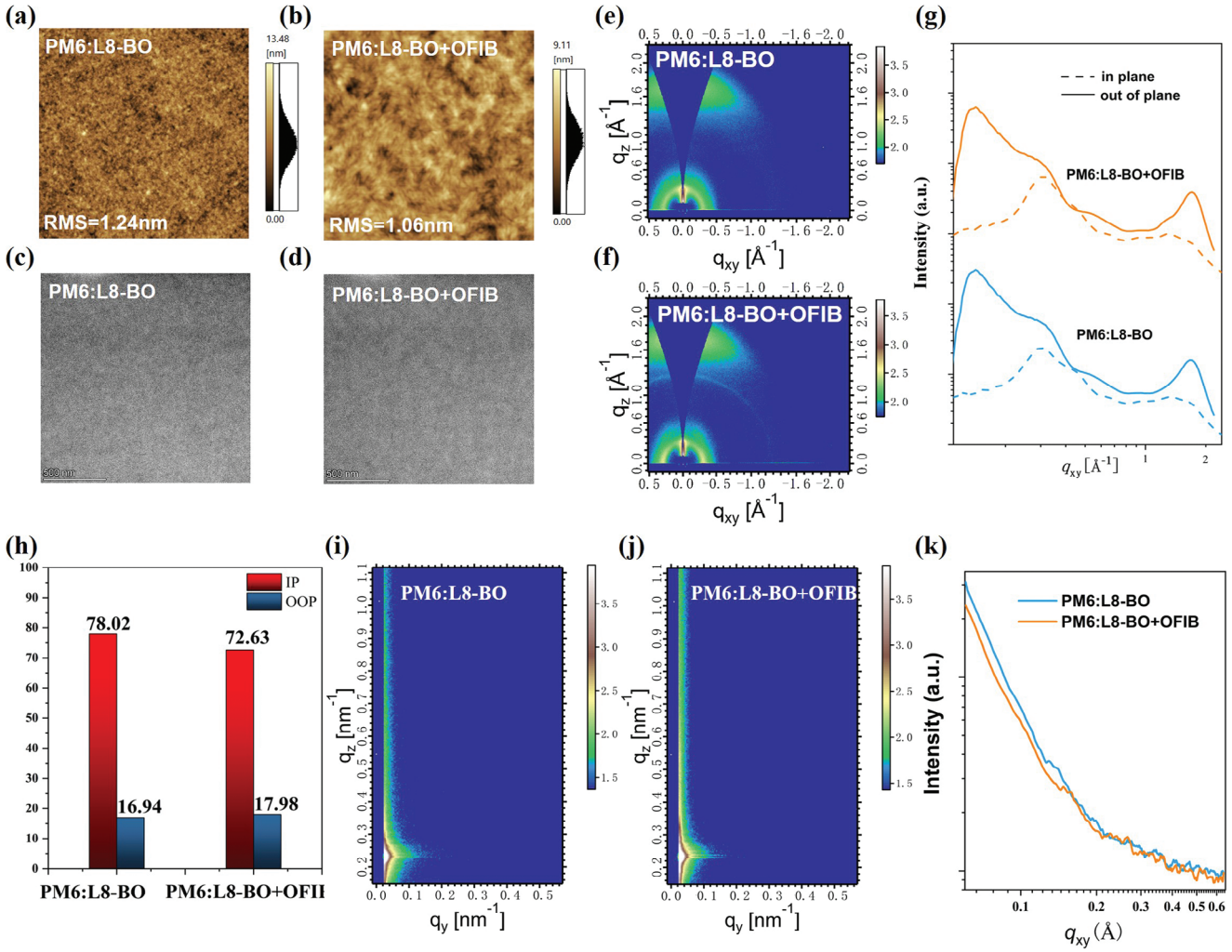

Figure 4. a–d) Atomic force microscopy (AFM; 5 × 5 µm; a,b) and transmission electron microscopy (TEM; c,d) images; e–g) Grazing incidence wide-angle X-ray scattering (GIWAXS) profiles of control and OFIB-processed blend film; h) IP and OOP intensity of the PM6:L8-BO and PM6:L8-BO+OFIB from the GIWAXS profiles; i–k) Grazing incidence wide-angle X-ray scattering (GISAXS) profiles of the corresponding films along the q_{xy} axis. All the blend films were prepared under the optimal conditions, and volume ratio of OFIB to PM6:L8-BO chloroform solution was 0.65%.

films. The first peak of $g(r)$ exhibited a significant increase in the probability or proportion of L8-BO distribution around L8-BO at ≈0.37 nm in the OFIB-processed blend. However, for the controlled system, although the first peak appeared at 0.34 nm, its $g(r)$ value was smaller than the first $g(r)$ distribution in the OFIB-processed blend system, the second small $g(r)$ peak appearing at ≈0.68 nm and with many different small peaks appearing at larger r values. That indicated a disorderly molecular orientation in the controlled system. These results indicated that the molecular packing became more ordered, which was consistent with the GIWAXS and GISAXS results.[68–71] Meanwhile, from the MD simulation results of 0.5% PFIB and 0.65% MFIB processed PM6:L8-BO processed blend films, both PFIB and MFIB exhibited relatively poor molecular packing compared with OFIB, as shown in Figure S18, Supporting Information. Raman mapping experiments revealed that the presence of OFIB promoted the attainment of an equilibrium state in the blend system. This state was characterized by a more homogeneous distribution in the vertical orientation and a suitable phase separation morphology, as displayed in Figure 5f–h.

To better understand how the OFIB influences the intrinsic photophysical processes of the devices, we used femtosecond transient absorption (fs-TA) spectroscopy to investigate the photophysical processes of the blend films.[72–75] In the experiments, we chose 800 nm pump light to excite the blend films and pure L8-BO, and 400 nm pump light to excite pure PM6 film. When the blend films were excited by 800 nm light, only L8-BO in the blend was excited. The measured fs-TA spectra, shown in **Figure 6**a,d, exhibit ground-state bleaching (GSB) signals at 550–640 and 680–850 nm for both blend films, respectively. The GSB signals at 550–640 nm correspond to PM6, whereas those at 680–850 nm correspond to L8-BO compared with the neat PM6 and L8-BO film (Figure S19, Supporting Information). The observed signal resulted from the complex overlap of multiple processes because the fs-TA spectrum signals originated from both the donor and acceptor materials after excitation. To be different with the neat

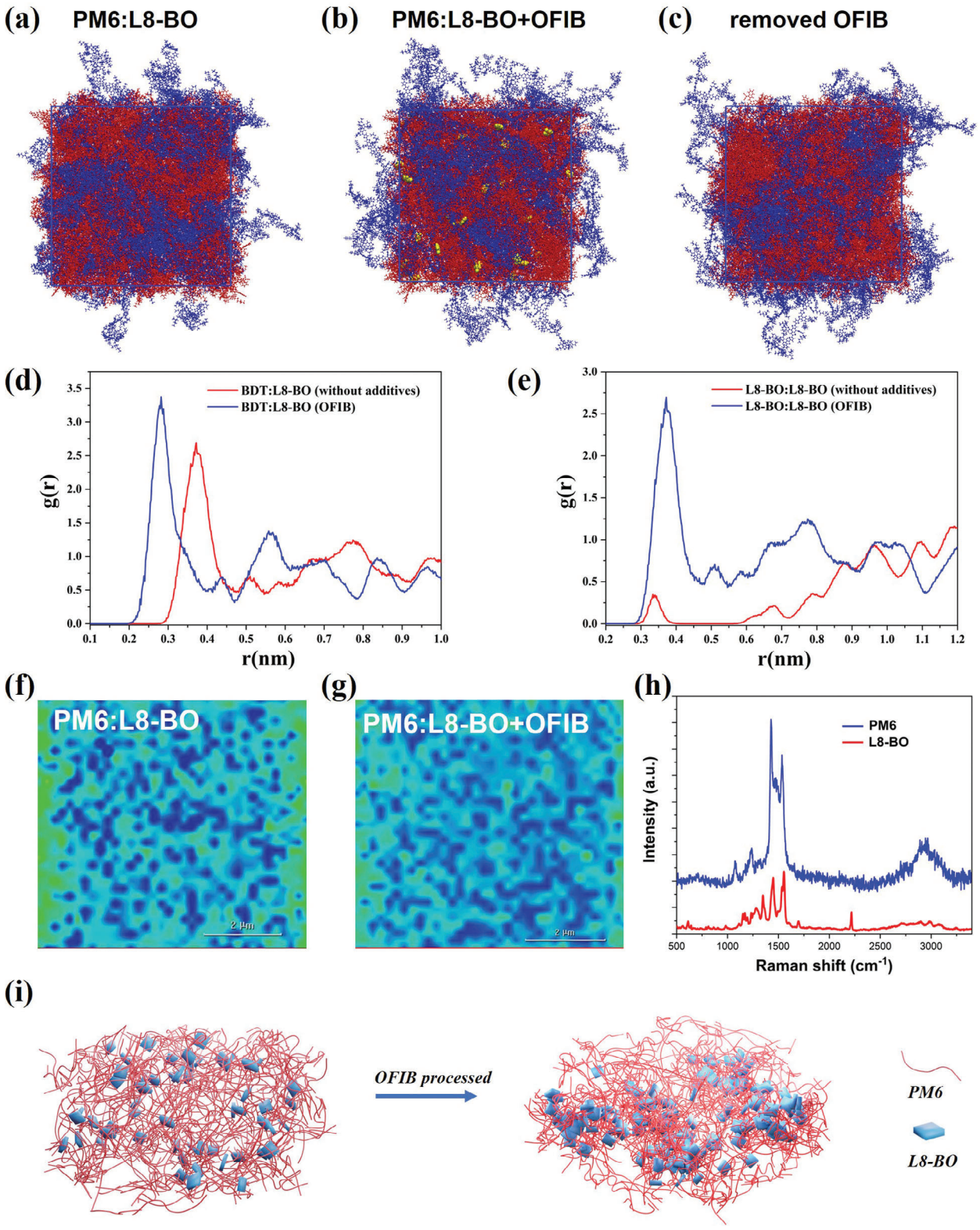

Figure 5. a–c) Shows the final snapshots of the control blend, blend film without the OFIB, and blend film with the OFIB removed, respectively; the red, blue, and yellow regions represent the L8-BO, PM6, and OFIB molecules, respectively. d,e) Center-of-mass radial distribution functions (RDF) of the acceptor L8-BO and BDT unit of the PM6, and L8-BO and L8-BO for the simulated films, respectively; f,g) The mapping image of control and OFIB-processed blend film based on confocal Raman spectroscopy (6 μm × 6 μm, step size is 0.1 μm, blue and red color regions PM6 and L8-BO, respectively); (h) is the Raman signals of neat PM6 and L8-BO film. i) Shows the molecular packing sketch maps of the control and OFIB-processed films.

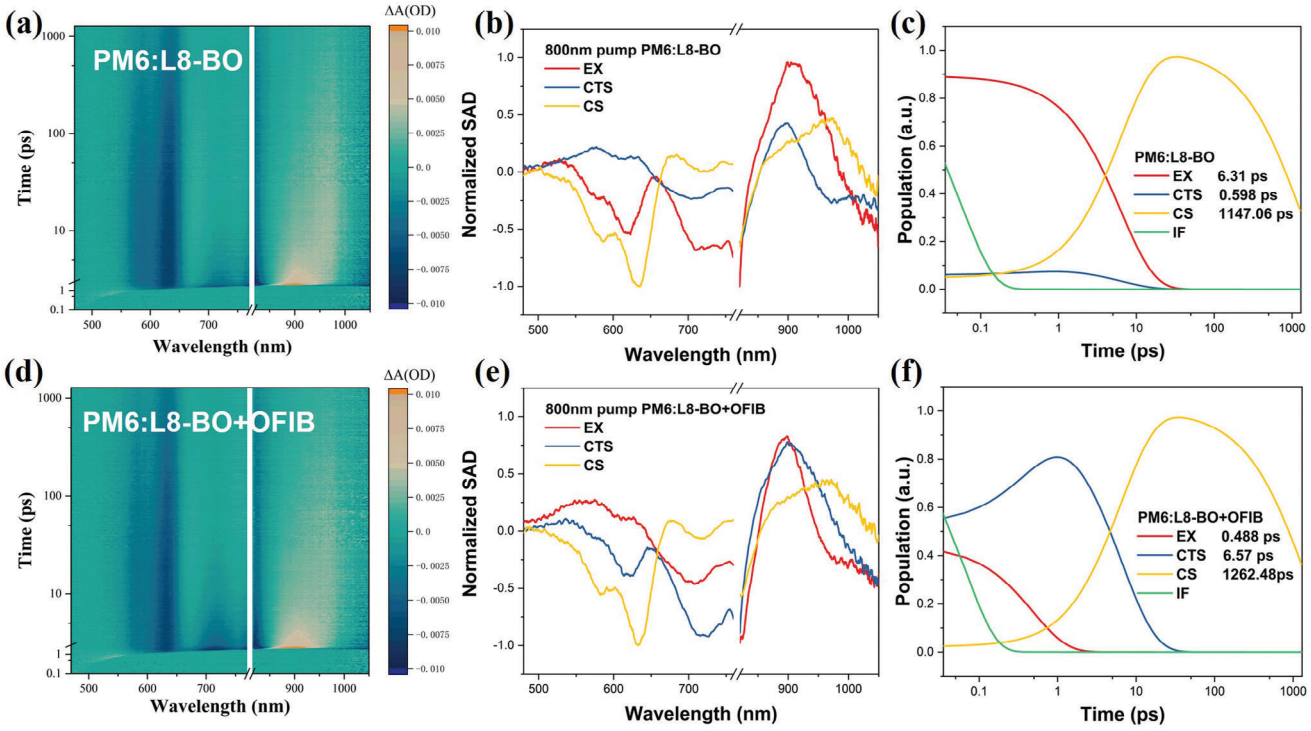

Figure 6. a,d) Shows the femtosecond transient absorption (fs-TAS) of the PM6:L8-BO and PM6:L8-BO+OFIB films; b,e) Shows the differences in the species-associated (SAD) spectra; and c,f) Shows the population versus time curves. All the blend films were prepared under the optimal conditions, and volume ratio of OFIB to PM6:L8-BO chloroform solution was 0.65%.

films, the charge separation state could be produced in the blend film because of the potential difference of the donor/acceptor interface. Before recombination back to the ground state, parts of excited excitons could exist in the form of charge transfer state and charge separation state in the blend film. For this reason, we utilized singular value decomposition and a global fitting algorithm to extract the dominant photophysical processes. Through this analysis, we successfully identified the populations and kinetic processes of three distinct species: exciton generation (EX), charge transfer state (CTS), and charge-separated (CS) states (Figure 6b,e). As shown by Figure S20 (Supporting Information), the characteristic spectrum of EX showed the similar shape with the GSB signals in neat PM6 and L8-BO films, verifying the reliability of the assignments of the species. The population of the species exhibited a substantial difference between the photophysical processes of the control and OFIB-processed blend films. For the control blend film, the lifetime of CTS (0.598 ps) was much shorter than that of the OFIB-processed blend film with CTS (6.57 ps). In addition, the EX lifetimes of the control and OFIB-processed blend films were 6.31 and 0.488 ps, respectively. After excitation, the blended films generated excitons, which typically underwent a transition from the CT state to the CS state. In the control-blend film, the population of EX excitons was much higher than that of CTS excitons in the initial state of excitation, and the lifetime of CTS was very short. In contrast, the OFIB-processed blend films have a lower population of EX excitons than that of CTS excitons, and their lifetimes were longer. However, the CS state populations in both blended films showed similar results, with the OFIB-processed blend exhibiting a longer CS state lifetime.

Based on our previous research work,[74] excitons had the probability of transitioning directly to the CS without passing through the CTS. Therefore, based on the current results, we propose an exciton competition mechanism for this system. The reaction rate, concentration of reactants and products, and reaction equilibrium principle collectively influence the equilibrium dynamics. EX excitons could pass through the CTS state and transition into the CS state. Additionally, both EX and CTS excitons could be directly transformed into the CS state. If the EX → CTS pathway was obstructed, the population of EX excitons accumulated, and promotion of the EX → CS pathway occurred, as depicted in Figure 6c. This could be attributed to the poor phase separation between the donor and acceptor, which was not conducive to the formation of CT excitons. In addition, trap-assisted recombination exacerbated the recombination of the CTS excitons. For OFIB-processed blend films, the phase separation size and molecular packing were optimized through additive control, facilitating the rapid generation of CT excitons. Consequently, the EX → CTS → CS pathway dominated at a higher percentage than the recombination of excitons. Figure 6f shows that the EX and CTS excitons occupied distinct populations in the initial state after excitation. Subsequently, the EX excitons rapidly converted almost entirely to the CTS state and then transitioned to the CS state. This implied that the additive effectively reduced the probability of exciton recombination.

3. Conclusion

In conclusion, our study elucidates the vital role of solvent additives in inducing better phase-separation of the donor and acceptor in the active layer. This serves as the fundamental basis for achieving enhanced phase separation and charge-transfer performance in PSCs, thereby determining their PCE. Specifically, our investigation focused on a structurally simple solvent additive, OFIB. We revealed its effective regulation of the active layer morphology, resulting in the formation of fibrous assemblies and a substantial increase in PCE from 16.34% to 18.38% based on the PM6:L8-BO system. Unlike other halogen-containing solvent additives that operate through dipole-induced mechanisms, OFIBs exhibit distinct behavior because of multiple electron conjugations between their I atoms and the conjugated framework in the active layer. This allows OFIB to establish nearly equal-strength π–π interactions with the conjugated frameworks of both the donor and acceptor materials. OFIB functions as a crystallization nucleus in the solvent evaporating process and induces the crystallization of the donor and acceptor. Complementary molecular dynamics simulations and characterization techniques such as GIWAXS and GISAXS provide valuable insights into OFIB-processed blends. These studies revealed a significant alignment of acceptor molecules, leading to enhanced overall π–π stacking within the active layer. Furthermore, femtosecond-timescale photophysical investigations demonstrated that the OFIB-optimized active layer exhibited reduced exciton losses at the donor–acceptor interface, further contributing to improved device performance. Overall, our findings not only offer a novel understanding of the underlying mechanisms governing solvent additives, but also present a comprehensive research methodology that can guide the development of next-generation NFAs for efficient PSCs. This study contributes to the advancement of PSC technology and paves the way for designing and optimizing high-performance solar cell materials in the future.

Supporting Information

Supporting Information is available from the Wiley Online Library or from the author.

Acknowledgements

This work was supported by the National Natural Science Foundation of China (Grant No. 62027822) and the National R&D Program of China (Grant No. 2019YFA0706402).

Conflict of Interest

The authors declare no conflict of interest.

Data Availability Statement

The data that support the findings of this study are available in the supplementary materials of this article.

Keywords

1-fluoro-2-iodobenzene, donor–acceptor interface, fibrous morphology, induced crystallization, molecular dynamics, polymer solar cells

Received: August 31, 2023
Revised: November 16, 2023
Published online:

[1] G. Yu, J. Gao, J. C. Hummelen, F. Wudl, A. J. Heeger, *Science* **1995**, *270*, 1789.
[2] M. C. Scharber, D. Mühlbacher, M. Koppe, P. Denk, C. Waldauf, A. J. Heeger, C. J. Brabec, *Adv. Mater.* **2006**, *18*, 789.
[3] J. Wang, Y. Cui, Y. Xu, K. Xian, P. Bi, Z. Chen, K. Zhou, L. Ma, T. Zhang, Y. Yang, Y. Zu, H. Yao, X. Hao, L. Ye, J. Hou, J. Hou, *Adv. Mater.* **2022**, *34*, 2205009.
[4] Y. Cui, H. Yao, J. Zhang, K. Xian, T. Zhang, L. Hong, Y. Wang, Y. Xu, K. Ma, C. An, C. He, Z. Wei, F. Gao, J. Hou, J. Hou, *Adv. Mater.* **2020**, *32*, 1908205.
[5] X. Liu, Y. Peng, Z. Liang, L. Wang, S. Han, Z. Dou, X. Lu, J. Tong, J. Liu, J. Li, *J. Mater. Chem. C* **2023**, *11*, 2871.
[6] Z. Liang, J. Tong, H. Li, Y. Wang, N. Wang, J. Li, C. Yang, Y. Xia, *J. Mater. Chem. A* **2019**, *7*, 15841.
[7] Y. Wang, Z. Liang, X. Liang, X. Wen, Z. Cai, Z. Shao, J. Zhang, Y. Ran, L. Yan, G. Lu, F. Huang, L. Hou, *Adv. Energy Mater.* **2023**, *13*, 2300524.
[8] G. Ding, T. Chen, M. Wang, X. Xia, C. He, X. Zheng, Y. Li, D. Zhou, X. Lu, L. Zuo, Z. Xu, H. Chen, *Nano-Micro Lett.* **2023**, *15*, 92.
[9] H. Chen, Z.-G. Zhang, F. Gao, *Sci. China Mater.* **2023**, *66*, 2523.
[10] F. Lu, S. Fu, L. Wang, S. Du, Z. Dou, X. Yang, J. Li, *Opt. Mater.* **2023**, *139*, 113782.
[11] M. A. Mubarok, H. Aqoma, F. T. A. Wibowo, W. Lee, H. M. Kim, D. Y. Ryu, J.-W. Jeon, S.-Y. Jang, *Adv. Energy Mater.* **2020**, *10*, 1902933.
[12] C. Zhu, J. Tian, W. Liu, Y. Duan, Y. Song, Z. You, X. Wang, N. Li, X. Zhan, T. P. Russell, Y. Liu, *ACS Energy Lett.* **2023**, *8*, 2689.
[13] R. Sun, J. Guo, Q. Wu, Z. Zhang, W. Yang, J. Guo, M. Shi, Y. Zhang, S. Kahmann, L. Ye, X. Jiao, M. A. Loi, Q. Shen, H. Ade, W. Tang, C. J. Brabec, J. Min, J. Min, *Energy Environ. Sci.* **2019**, *12*, 3118.
[14] J. Tong, S. Xiong, Y. Zhou, L. Mao, X. Min, Z. Li, F. Jiang, W. Meng, F. Qin, T. Liu, R. Ge, C. Fuentes-Hernandez, B. Kippelen, Y. Zhou, *Mater. Horiz.* **2016**, *3*, 452.
[15] H. Tang, Y. Bai, H. Zhao, X. Qin, Z. Hu, C. Zhou, F. Huang, Y. Cao, *Adv. Mater.* **2023**, 2212236.
[16] L. Kong, Z. Zhang, N. Zhao, Z. Cai, J. Zhang, M. Luo, X. Wang, M. Chen, W. Zhang, L. Zhang, Z. Wei, J. Chen, *Adv. Energy Mater.* **2023**, *13*, 2300763.
[17] B. Fan, W. Zhong, W. Gao, H. Fu, F. Lin, R. Wong, M. Liu, C. Zhu, C. Wang, H. Yip, F. Liu, A. Jen, *Adv. Mater.* **2023**, *35*, 1302861.
[18] Y. Zhang, Y. Ji, Y. Zhang, W. Zhang, H. Bai, M. Du, H. Wu, Q. Guo, E. Zhou, *Adv. Funct. Mater.* **2022**, *32*, 2205115.
[19] M. Saladina, P. S. Marqués, A. Markina, S. Karuthedath, C. Wöpke, C. Göhler, Y. Chen, M. Allain, P. Blanchard, C. Cabanetos, D. Andrienko, F. Laquai, J. Gorenflot, C. Deibel, *Adv. Funct. Mater.* **2021**, *31*, 2007479.
[20] Y. Ji, H. Bai, L. Zhang, Y. Zhang, L. Ding, *J. Semicond.* **2022**, *43*, 050203.
[21] Y. Wang, Z. Liang, X. Li, J. Qin, M. Ren, C. Yang, X. Bao, Y. Xia, J. Li, *J. Mater. Chem. C* **2019**, *7*, 11152.
[22] L. Sang, X. Chen, J. Fang, P. Xu, W. Tian, K. Shui, Y. Han, H. Wang, R. Huang, Q. Zhang, Q. Luo, C.-Q. Ma, *Adv. Funct. Mater.* **2023**, *33*, 2304824.
[23] J. Shi, Z. Chen, H. Liu, Y. Qiu, S. Yang, W. Song, Z. Ge, *Adv. Energy Mater.* **2023**, *13*, 1301292.
[24] F. Cheng, Y. Cui, F. Ding, Z. Chen, Q. Xie, X. Xia, P. Zhu, X. Lu, H. Zhu, X. Liao, Y. Chen, *Adv. Mater.* **2023**, *35*, 2300820.
[25] A. Khasbaatar, Z. Xu, J.-H. Lee, G. Campillo-Alvarado, C. Hwang, B. N. Onusaitis, Y. Diao, *Chem. Rev.* **2023**, *123*, 8395.
[26] H. Laval, A. Holmes, M. A. Marcus, B. Watts, G. Bonfante, M. Schmutz, E. Deniau, R. Szymanski, C. Lartigau-Dagron, X. Xu, J. M.

Cairney, K. Hirakawa, F. Awai, T. Kubo, G. Wantz, A. Bousquet, N. P. Holmes, S. Chambon, *Adv. Energy Mater.* **2023**, *13*, 2300249.
[27] H. Yao, Y. Li, H. Hu, P. C. Y. Chow, S. Chen, J. Zhao, Z. Li, J. H. Carpenter, J. Y. L. Lai, G. Yang, Y. Liu, H. Lin, H. Ade, H. Yan, *Adv. Energy Mater.* **2018**, *8*, 1701895.
[28] K. Jiang, J. Zhang, Z. Peng, F. Lin, S. Wu, Z. Li, Y. Chen, H. Yan, H. Ade, Z. Zhu, A. K.-Y. Jen, *Nat. Commun.* **2021**, *12*, 468.
[29] Z. Wang, Y. Hu, T. Xiao, Y. Zhu, X. Chen, L. Bu, Y. Zhang, Z. Wei, B. B. Xu, G. Lu, *Adv. Opt. Mater.* **2019**, *7*, 1900152.
[30] S. Yao, C. Huang, Q. Wang, T. Yang, S. Shi, Y. Liu, C. Zhao, Z. Zhang, X. Shen, T. Li, B. He, W. Lin, T. Zhang, B. Zou, T. Liu, *Sol. RRL* **2022**, *6*, 2200617.
[31] H. Hu, K. Jiang, J.-H. Kim, G. Yang, Z. Li, T. Ma, G. Lu, Y. Qu, H. Ade, H. Yan, *J. Mater. Chem. A* **2016**, *4*, 5039.
[32] J. Wu, Z. Ling, L. Franco, S. Jeong, Z. Genene, J. Mena, S. Chen, C. Chen, C. Araujo, C. Chang, F. Isikgor, Q. Chen, H. Han, F. Laquai, M. Zhang, H. Anthopoulos, E. Wang, *Angew. Chem., Int. Ed.* **2023**, *62*, 202302888.
[33] F. Wang, M. Li, Q. Tian, R. Sun, H. Ma, H. Wang, J. Chang, Z. Li, H. Chen, J. Cao, A. Wang, J. Dong, Y. Liu, J. Zhao, Y. Chu, S. Yan, Z. Wu, J. Liu, Y. Li, X. Chen, P. Gao, Y. Sun, T. Liu, W. Liu, R. Li, J. Wang, Y.-B. Cheng, X. Liu, W. Huang, T. Qin, *Nat. Commun.* **2023**, *14*, 3216.
[34] Y. Cai, Q. Li, G. Lu, H. S. Ryu, Y. Li, H. Jin, Z. Chen, Z. Tang, G. Lu, X. Hao, H. Y. Woo, C. Zhang, Y. Sun, *Nat. Commun.* **2022**, *13*, 2369.
[35] H.-C. Chou, W.-C. Hsu, Y. Yang, K. S. Schanze, S.-C. Luo, C. Chen, *Macromol. Chem. Phys.* **2021**, *222*, 2100135.
[36] R. K. Gupta, R. Garai, M. Hossain, M. A. Afroz, D. Kalita, P. K. Iyer, *J. Mater. Chem. C* **2021**, *9*, 8746.
[37] C. Cui, Y. Li, *Aggregate* **2021**, *2*, 31.
[38] W. Li, M. Chen, Z. Zhang, J. Cai, H. Zhang, R. S. Gurney, D. Liu, J. Yu, W. Tang, T. Wang, *Adv. Funct. Mater.* **2019**, *29*, 1807662.
[39] L. Chen, J. Yi, R. Ma, L. Ding, T. A. D. Peña, H. Liu, J. Chen, C. Zhang, C. Zhao, W. Lu, Q. Wei, B. Zhao, H. Hu, J. Wu, Z. Ma, X. Lu, M. Li, G. Zhang, G. Li, H. Yan, *Adv. Mater.* **2023**, *35*, 2301231.
[40] J. Wang, Y. Wang, P. Bi, Z. Chen, J. Qiao, J. Li, W. Wang, Z. Zheng, S. Zhang, X. Hao, J. Hou, J. Hou, *Adv. Mater.* **2023**, *35*, 2301583.
[41] K. Kim, J. Han, S. Lee, S. Kim, J.-M. Choi, J.-S. Nam, D. Kim, I. Chung, T.-D. Kim, S. Manzhos, S. J. Choi, J. W. Song, D. S. Kim, J. Y. Do, I. Jeon, *Adv. Energy Mater.* **2023**, *13*, 2203742.
[42] X. Yuan, H. Chen, S. Kim, Y. Chen, Y. Zhang, M. Yang, Z. Chen, C. Yang, H. Wu, X. Gao, Z. Liu, C. Duan, *Adv. Energy Mater.* **2023**, *13*, 2204394.
[43] Z. Ding, Y. Zhang, Y. Su, Y. Wu, Y. Han, K. Zhao, S. Liu, *Energy Environ. Mater.* **2023**, *6*, e12421.
[44] D. H. Lee, D. H. Kim, T. Kim, D. C. Lee, S. Cho, T. Park, *Nano Energy* **2022**, *93*, 106878.
[45] J. Ko, J. Kim, H.-J. Song, Y. Park, J. Kwak, C. Lee, K. Char, *Adv. Mater. Interfaces* **2021**, *8*, 2100029.
[46] J. Liu, S. Zeng, P. Jing, K. Zhao, Q. Liang, *J. Energy Chem.* **2020**, *51*, 333.
[47] C. Liu, X. Du, S. Gao, A. Classen, A. Osvet, Y. He, K. Mayrhofer, N. Li, C. J. Brabec, *Adv. Energy Mater.* **2020**, *10*, 1903800.
[48] S. Li, Q. Ma, S. Chen, L. Meng, J. Zhang, Z. Zhang, C. Yang, Y. Li, *J. Mater. Chem. C* **2020**, *8*, 15296.
[49] J. Cai, H. Wang, X. Zhang, W. Li, D. Li, Y. Mao, B. Du, M. Chen, Y. Zhuang, D. Liu, H.-L. Qin, Y. Zhao, J. A. Smith, R. C. Kilbride, A. J. Parnell, R. A. L. Jones, D. G. Lidzey, T. Wang, *J. Mater. Chem. A* **2020**, *8*, 4230.
[50] L. Zhu, W. Zhong, C. Qiu, B. Lyu, Z. Zhou, M. Zhang, J. Song, J. Xu, J. Wang, J. Ali, W. Feng, Z. Shi, X. Gu, L. Ying, Y. Zhang, F. Liu, *Adv. Mater.* **2019**, *31*, 1902899.
[51] R. Yu, H. Yao, L. Hong, Y. Qin, J. Zhu, Y. Cui, S. Li, J. Hou, J. Hou, *Nat. Commun.* **2018**, *9*, 4645.
[52] X. Song, K. Zhang, R. Guo, K. Sun, Z. Zhou, S. Huang, L. Huber, M. Reus, J. Zhou, M. Schwartzkopf, S. V. Roth, W. Liu, Y. Liu, W. Zhu, P. Müller-Buschbaum, *Adv. Mater.* **2022**, *34*, 2200907.
[53] Q. Lai, R. Zhuang, K. Zhang, T. Wu, L. Xie, R. Zhao, L. Yang, Y. Wang, Y. Hua, *Angew. Chem., Int. Ed.* **2023**, *62*, 202305670.
[54] W. Xue, Z. Liang, Y. Tang, C. Zhao, L. Yan, W. Ma, H. Yan, *Adv. Funct. Mater.* **2023**, *33*, 2304960.
[55] H. Liu, Y. Fu, Z. Chen, J. Wang, J. Fu, Y. Li, G. Cai, C.-J. Su, U.-S. Jeng, H. Zhu, G. Li, X. Lu, *Adv. Funct. Mater.* **2023**, *33*, 2303307.
[56] S. A. Park, D. H. Kim, D. Chung, J. Kim, T. Park, S. Cho, M. Kim, *ACS Appl. Mater. Interfaces* **2023**, *15*, 27026.
[57] S. Duan, S.-I. Sasaki, D. Han, G. Zhang, D. Li, C. Feng, X.-F. Wang, H. Tamiaki, S. Chung, K. Cho, G. Li, S. Lu, *Adv. Funct. Mater.* **2023**, *33*, 2302820.
[58] Z. Shen, J. Yu, G. Lu, K. Wu, Q. Wang, L. Bu, X. Liu, Y. Zhu, G. Lu, *Energy Environ. Sci.* **2023**, *16*, 2945.
[59] H. Quan, Z. Zhong, T. Hao, K. An, W. Zhong, C. Wang, F. Liu, L. Ying, F. Huang, *Chem. Eng. J.* **2023**, *452*, 139295.
[60] L. Zhu, M. Zhang, G. Zhou, T. Hao, J. Xu, J. Wang, C. Qiu, N. Prine, J. Ali, W. Feng, X. Gu, Z. Ma, Z. Tang, H. Zhu, L. Ying, Y. Zhang, F. Liu, *Adv. Energy Mater.* **2020**, *10*, 1904234.
[61] J. Li, Z. Liang, Y. Wang, H. Li, J. Tong, X. Bao, Y. Xia, *J. Mater. Chem. C* **2018**, *6*, 11015.
[62] G.-J. A. H. Wetzelaer, M. Kuik, Y. Olivier, V. Lemaur, J. Cornil, S. Fabiano, M. A. Loi, P. W. M. Blom, *Phys. Rev. B* **2012**, *86*, 165203.
[63] K. Vandewal, K. Tvingstedt, A. Gadisa, O. Inganäs, J. V. Manca, *Phys. Rev. B* **2010**, *81*, 125204.
[64] T. J. K. Brenner, I. Hwang, N. C. Greenham, C. R. Mcneill, *J. Appl. Phys.* **2010**, *107*, 114501.
[65] L. A. A. Pettersson, L. S. Roman, O. Inganäs, *J. Appl. Phys.* **1999**, *86*, 487.
[66] T. Liu, L. Huo, S. Chandrabose, K. Chen, G. Han, F. Qi, X. Meng, D. Xie, W. Ma, Y. Yi, J. M. Hodgkiss, F. Liu, J. Wang, C. Yang, Y. Sun, *Adv. Mater.* **2018**, *30*, 1707353.
[67] G. Han, Y. Guo, R. Duan, X. Shen, Y. Yi, *J. Mater. Chem. A* **2017**, *5*, 9316.
[68] S. Jung, Y. Cho, Y. Ji, J. Oh, G. Park, W. Kim, S. Jeong, S. M. Lee, S. Chen, Y. Zhang, C. Yang, *Nano Energy* **2023**, *106*, 108059.
[69] S. Lee, G. Park, M. Jeong, B. Lee, S. Jeong, J. Park, Y. Cho, S. M. Noh, C. Yang, *ACS Appl. Mater. Interfaces* **2022**, *14*, 33614.
[70] T. L. H. Mai, S. Jeong, S. Kim, S. Jung, J. Oh, Z. Sun, J. Park, S. Lee, W. Kim, C. Yang, *Adv. Funct. Mater.* **2023**, *33*, 2303386.
[71] L. Zhong, Z. Sun, S. Lee, S. Jeong, S. Jung, Y. Cho, J. Park, J. Park, S.-J. Yoon, C. Yang, *Adv. Funct. Mater.* **2023**, *33*, 2305450.
[72] P. Gong, P. Guo, Y. Wang, L. Yan, Z. Liang, M. Ding, J. Tong, J. Li, Y. Xia, *ACS Appl. Energy Mater.* **2021**, *4*, 9627.
[73] J. Li, Z. Liang, X. Li, H. Li, Y. Wang, J. Qin, J. Tong, L. Yan, X. Bao, Y. Xia, *ACS Appl. Mater. Interfaces* **2020**, *12*, 8475.
[74] L. Yan, Z. Liang, J. Si, P. Gong, Y. Wang, X. Liu, J. Tong, J. Li, X. Hou, *ACS Appl. Mater. Interfaces* **2022**, *14*, 6945.
[75] Z. Chen, C. He, P. Ran, X. Chen, Y. Zhang, C. Zhang, R. Lai, Y. (M). Yang, H. Chen, H. Zhu, *Energy Environ. Sci.* **2023**, *16*, 3373.